

# J021659-044920: a relic giant radio galaxy at $z \sim 1.3$

P. Tamhane,<sup>1,2\*</sup> Y. Wadadekar,<sup>2†</sup> A. Basu,<sup>3</sup> V. Singh,<sup>4</sup> C. H. Ishwara-Chandra,<sup>2</sup>  
A. Beelen<sup>5</sup>, and S. Sirothia<sup>2,6,7</sup>

<sup>1</sup>Indian Institute of Science Education and Research, Dr Homi Bhabha Road, Pashan, Pune 411008, India

<sup>2</sup>National Centre for Radio Astrophysics, TIFR, Post Bag 3, Ganeshkhind, Pune 411007, India

<sup>3</sup>Max-Planck-Institut für Radioastronomie, Auf dem Hügel 69, D-53121 Bonn, Germany

<sup>4</sup>Astrophysics and Cosmology Research Unit, School of Chemistry and Physics, University of KwaZulu-Natal, Durban 4000, South Africa

<sup>5</sup>Institut d'Astrophysique Spatiale, Bât. 121, Université Paris-Sud, F-91405 Orsay Cedex, France

<sup>6</sup>Square Kilometre Array South Africa, 3rd Floor, The Park, Park Road, Pinelands, 7405, South Africa

<sup>7</sup>Department of Physics and Electronics, Rhodes University, PO Box 94, Grahamstown 6140, South Africa

Published in MNRAS; volume 453, issue 3, pages 2438–2446

## ABSTRACT

We report the discovery of a relic Giant Radio Galaxy (GRG) J021659-044920 at redshift  $z \sim 1.3$  that exhibits large-scale extended, nearly co-spatial, radio and X-ray emission from radio lobes, but no detection of Active Galactic Nuclei core, jets and hotspots. The total angular extent of the GRG at the observed frame 0.325 GHz, using Giant Metrewave Radio Telescope observations is found to be  $\sim 2.4$  arcmin, that corresponds to a total projected linear size of  $\sim 1.2$  Mpc. The integrated radio spectrum between 0.240 and 1.4 GHz shows high spectral curvature ( $\alpha_{0.610 \text{ GHz}}^{1.4 \text{ GHz}} - \alpha_{0.240 \text{ GHz}}^{0.325 \text{ GHz}} > 1.19$ ) with sharp steepening above 0.325 GHz, consistent with relic radio emission that is  $\sim 8 \times 10^6$  yr old. The radio spectral index map between observed frame 0.325 and 1.4 GHz for the two lobes varies from 1.4 to 2.5 with the steepening trend from outer-end to inner-end, indicating backflow of plasma in the lobes. The extended X-ray emission characterized by an absorbed power-law with photon index  $\sim 1.86$  favours inverse-Compton scattering of the Cosmic Microwave Background (ICCMB) photons as the plausible origin. Using both X-ray and radio fluxes under the assumption of ICCMB we estimate the magnetic field in the lobes to be  $3.3 \mu\text{G}$ . The magnetic field estimate based on energy equipartition is  $\sim 3.5 \mu\text{G}$ . Our work presents a case study of a rare example of a GRG caught in dying phase in the distant Universe.

**Key words:** galaxies: active – galaxies: individual: J021659-044920 – galaxies: jets – radio continuum: galaxies – X-rays: galaxies

## 1 INTRODUCTION

The radio morphology of a radio galaxy typically consists of a core, a pair of highly collimated jets and lobes formed by the supply of relativistic plasma from Active Galactic Nuclei (AGN; Scheuer 1974; Begelman et al. 1984; Bridle & Perley 1984). A less common population of radio galaxies with total linear size larger than  $\sim 0.7$  Mpc is referred as Giant Radio Galaxies (GRGs; e.g. Saripalli et al. 2005). After an active phase, which lasts for  $\sim 10^7 - 10^8$  yr, the AGN activity stops or falls to very low level such that the outflowing jets are no longer sustained. As a result, the core, jets and hotspots on the lobes disappear. However, the lobes can be seen for

relatively shorter period of time ( $10^6 - 10^7$  yr) before they disappear due to radiative losses (Murgia et al. 2011). Thus, a relic radio galaxy resulting from the cessation of AGN activity represents a short-lived final phase of radio galaxy evolution. The short-lived phase makes them a rare class of objects.

The switch off of fresh particle injection leads to an exponential steepening of the radio spectrum in the radio lobes, resulting in a much steeper spectrum ( $\alpha > 1.3$ ) than that of normal radio galaxies (Komissarov & Gubanov 1994). The low surface brightness and very steep radio spectrum makes relic GRGs ideally suited to be detected and studied at low frequencies. However, despite concerted efforts to search for relic radio galaxies, hitherto, only a handful of such objects have been reported in the literature (e.g. Cordey 1987; Venturi et al. 1998; Murgia et al. 2005, 2011;

\* E-mail: ptamhane@students.iiserpune.ac.in

† E-mail: yogesh@ncra.tifr.res.in

Hurley-Walker et al. 2015). In this paper, we report the discovery of a relic GRG J021659-044920 using deep 0.325 and 1.4 GHz observations carried out at the Giant Metrewave Radio Telescope (GMRT) and the Very Large Array (VLA), respectively.

The reported relic GRG lies in the *XMM*-Large Scale Structure (*XMM*-LSS) field. The existing X-ray data from *XMM-Newton* show extended X-ray emission nearly co-spatial with the radio lobes. A variety of physical processes can give rise to extended X-ray emission such as thermal emission from shocks, synchrotron radiation and inverse-Compton (IC) scattering of the ubiquitous Cosmic Microwave Background (CMB) photons. Indeed, IC scattered CMB photons have been detected in the form of diffuse, extended X-ray emission in several radio galaxies at redshift  $z > 1$  [e.g. 4C41.17 (Scharf et al. 2003), 3C 294 (Fabian et al. 2003), 6C 0905+39 (Blundell et al. 2006; Erlund et al. 2008), 4C 23.56 (Johnson et al. 2007), and HDF-130 (Fabian et al. 2009), 3C 469.1 and MRC 2216–206 (Laskar et al. 2010)]. However, given the dearth of relic GRGs and their X-ray observations, X-ray properties of relic GRGs are poorly studied. For example, only 2 out of 11 relic radio galaxies in Parma et al. (2007) and three out of five relic radio galaxies in Murgia et al. (2011) sample have X-ray studies. For the relic GRG J021659-044920, we use radio and X-ray observations to study its properties e.g., morphology, dominant energy loss processes, energetics and magnetic field strength.

In Section 2, we discuss the multiwavelength data used in our study. In Section 3, we present the radio morphology and spectral properties of the source. The X-ray emission properties are discussed in Section 4. In Section 5, we discuss the connection between the radio and X-ray emission. We estimate the magnetic field strength and the spectral age of the relic lobes in Section 6. We summarize our results in Section 7.

Throughout the paper, spectral index is defined as  $S_\nu \propto \nu^{-\alpha}$ . We use the *Wilkinson Microwave Anisotropy Probe* 9 cosmology with  $H_0 = 69.32 \text{ km s}^{-1} \text{ Mpc}^{-1}$ ,  $\Omega_m = 0.29$  and  $\Omega_\Lambda = 0.71$ . All the frequencies are in the observed frame unless mentioned otherwise.

## 2 OBSERVATIONS AND DATA ANALYSIS

The relic GRG J021659-044920 centred at RA  $02^{\text{h}} 16^{\text{m}} 59^{\text{s}}$  and Dec.  $-04^\circ 49' 20''.6$  (J2000) is located in a smaller subfield of the *XMM*-LSS field, known as the Subaru X-ray Deep Field (SXDF; Ueda et al. 2008). Both SXDF and *XMM*-LSS have excellent multiwavelength data coverage in X-ray, optical, near-infrared (IR), mid-IR and radio bands (Simpson et al. 2006; Vardoulaki et al. 2008; Mauduit et al. 2012). The details of the data used in our study are given below.

### 2.1 Radio data

#### 2.1.1 0.325 GHz data

We use a GMRT observation at 0.325 GHz to study the low-frequency radio properties of the relic GRG J021659-044920. We have carried out deep 0.325 GHz GMRT ob-

servations of the *XMM*-LSS field covering  $\sim 12 \text{ deg}^2$  over 16-pointings with 32 MHz bandwidth. The GMRT observations are taken in semisnapshot mode to optimize the *uv*-coverage. The GMRT map has average rms noise of  $\sim 150 \mu\text{Jy beam}^{-1}$  and angular resolution  $9.35 \text{ arcsec} \times 7.38 \text{ arcsec}$ . In Figure 1 (left-hand panel), we present the grey-scale image of the relic GRG studied in this paper. The details of the 0.325 GHz GMRT observations will be presented in Wadadekar et al. (in preparation). The 0.325 GHz GMRT observations in combination with the existing multiwavelength data in the *XMM*-LSS field, have already been used to study the population of ultrasteepest spectrum radio sources (Singh et al. 2014) and the radio-FIR correlation for distant star-forming galaxies (Basu et al. 2015).

#### 2.1.2 0.240 GHz and 0.610 GHz data

The *XMM*-LSS field was observed at 0.24 and 0.61 GHz using the GMRT by Tasse et al. (2007). The 0.240 and 0.610 GHz observations cover  $18.0$  and  $12.7 \text{ deg}^2$  with rms noise  $\sim 2.5$  and  $\sim 0.3 \text{ mJy beam}^{-1}$  and angular resolutions of  $14.7 \text{ arcsec}$  and  $6.5 \text{ arcsec}$ , respectively. The Integrated flux densities of the relic GRG reported in Tasse et al. (2007) are  $169.1 \pm 20.2$  and  $20.2 \pm 2.7 \text{ mJy}$  at 0.240 and 0.610 GHz, respectively. In a deeper GMRT observation of the SXDF at 0.610 GHz covering  $0.5 \text{ deg}^2$  with map rms noise of  $\sim 60 \mu\text{Jy beam}^{-1}$ , at a resolution of  $6.8 \text{ arcsec} \times 5.4 \text{ arcsec}$  by Vardoulaki et al. (2008), the total flux density of the source is found to be  $43.3 \text{ mJy}$ . This clearly shows that the low surface brightness emission is missed in the shallow observations reported in Tasse et al. (2007). We therefore use the 0.610 GHz flux density given in Vardoulaki et al. (2008) for our analysis.

#### 2.1.3 1.4 GHz data

A deep 1.4 GHz image of the source, observed using the VLA, is available from Simpson et al. (2006) who has surveyed the SXDF field covering  $0.8 \text{ deg}^2$ . The VLA observations were made using B- and C-array configuration and render rms noise of  $\sim 20 \mu\text{Jy beam}^{-1}$ , at  $\sim 5.0 \text{ arcsec} \times 4.0 \text{ arcsec}$  angular resolution. We show the 1.4 GHz contours in Figure 1 (right-hand panel).

#### 2.1.4 Missing flux density of radio emission

The total flux density from a large angular size source can be underestimated due to under sampling of the *uv*-plane at the shortest *uv*-distance. This could be significant at higher radio frequencies. An interferometer with the shortest baseline  $D_{\text{min}}$  can detect all the flux from angular scales less than  $\sim 0.6\lambda/D_{\text{min}}$ , provided the *uv*-plane is densely sampled at the shortest spacings. Here,  $\lambda$  is the observing wavelength. The total angular extent of the GRG is  $\sim 2.4 \text{ arcmin}$  at 0.325 GHz, and can be well sampled by baselines having *uv*-length  $\gtrsim 1 \text{ k}\lambda$ . This is not an issue with both the GMRT and VLA observations at 0.325 and 1.4 GHz, as the shortest baseline starts from  $\sim 0.15$  and  $\sim 0.17 \text{ k}\lambda$ , respectively. Hence, we do not expect any missing flux density at 0.325 and 1.4 GHz and all the structures are well recovered. Additionally, we compared the flux density at 1.4 GHz with NRAO VLA Sky

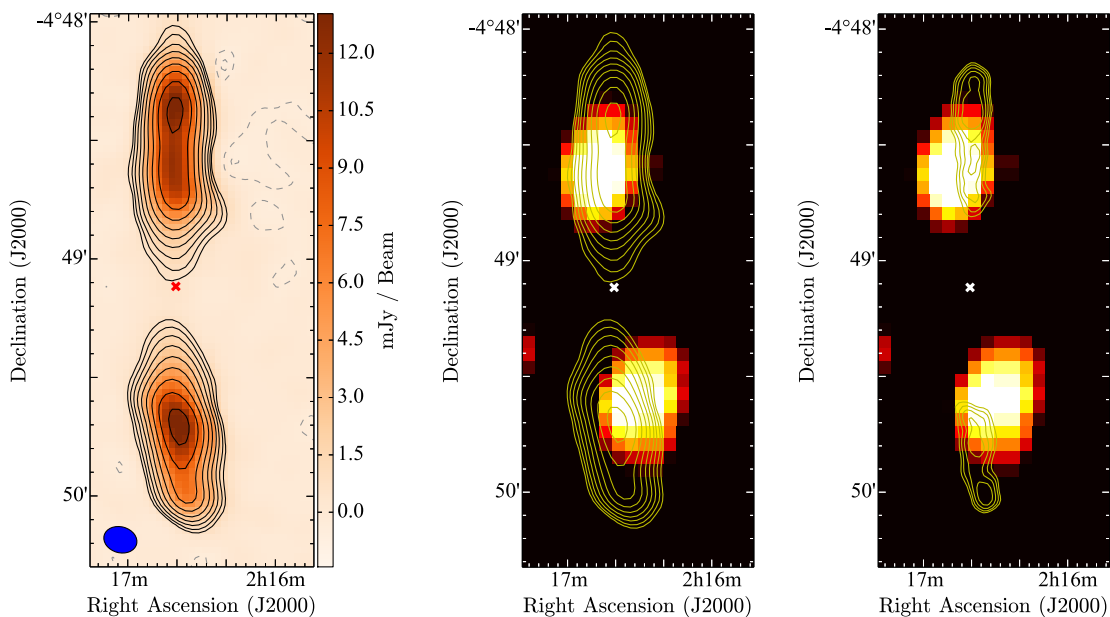


**Figure 1.** Left-hand panel: grey-scale image of the relic GRG J021659-044920 at 0.325 GHz observed using the GMRT having angular resolution of  $9.35 \text{ arcsec} \times 7.38 \text{ arcsec}$ . The map rms noise is  $\sim 150 \mu\text{Jy beam}^{-1}$ . Overlaid are the contours at 0.325 GHz starting from  $5\sigma$  increasing in steps of  $\sqrt{2} \times \sigma$ . The dashed grey contours are at  $-3\sigma$  and  $-2\sigma$ . Middle Panel: grey-scale image of the soft X-ray band (0.3–2.0 keV) EPIC PN from the *XMM–Newton*. Overlaid are the 0.325 GHz contours as in the left-hand panel. Right-hand panel: the soft X-ray band image overlaid with the 1.4 GHz contours starting from  $5\sigma$  increasing in steps of  $\sqrt{2} \times \sigma$ . The 1.4 GHz observation has angular resolution of  $\sim 5.0 \text{ arcsec} \times 4.0 \text{ arcsec}$  and rms noise of  $\sim 20 \mu\text{Jy beam}^{-1}$ . In both middle and right-hand panel, the X-ray image is smoothed with a Gaussian of kernel radius 5.0 arcsec. The marker ‘x’ indicates the position of the host galaxy.

Survey (NVSS). They were found to be comparable indicating negligible missing flux density.

Further, we note that the 0.610 GHz flux density measured by Vardoulaki et al. (2008) used baselines above 1.5 k $\lambda$  for their analysis. Thus, the flux density of 43.3 mJy at 0.61 GHz could be underestimated due to missing flux and hence is lower than the actual flux density.

## 2.2 X-ray data

We used *XMM–Newton* archival data with observation ID 0112372001. The data were taken in prime-full window mode using thin filter on 2003 January 7, and consist of 25.63 ks EPIC PN and 27.35 ks of EPIC MOS data. EPIC comprises a set of three X-ray CCD cameras i.e., two MOS cameras (Metal Oxide Semi-conductor CCD arrays) and one PN camera (pn CCD array). The EPIC cameras perform sensitive imaging observations in the energy range 0.15–15 keV with spatial resolution 4.0 arcsec – 6.0 arcsec and spectral resolution ( $E/\Delta E$ )  $\sim 20 - 50$  over the telescopes field of view of 30 arcmin (Strüder et al. 2001; Turner et al. 2001). The sensitivity of EPIC MOS/PN sharply declines above 10 keV resulting in inadequate counts above 10 keV for these observations. Figure 1 shows spatially smoothed EPIC-PN soft band (0.3 – 2.0 keV) X-ray image of the relic GRG. Overlaid are 0.325 GHz (middle panel) and 1.4 GHz (right-hand panel) radio contours. The soft X-ray image is smoothed with a Gaussian of kernel radius 5.0 arcsec. X-ray emission from extended diffuse double lobes of the relic GRG are clearly seen and are nearly co-spatial with

0.325 GHz lobe emission. We describe the details of X-ray data analysis in Section 4.

## 2.3 Optical, near-IR data and host galaxy identification

Simpson et al. (2006) present optical identifications for all radio sources detected in the 1.4 GHz imaging of the SXDF. The optical identifications of radio sources is based on the ultra-deep  $B$ ,  $R$ ,  $i'$ ,  $z'$  Suprime-Cam/Subaru images. The optical identifications were made by overlaying the radio contours on to a true-colour  $B$ ,  $R$ ,  $z'$  image. The relatively high resolution of the 1.4 GHz radio map allowed unambiguous identification with optical sources as there was typically only one source within an arcsecond of the peak of the radio emission, even at extremely faint optical magnitudes. For sources composed of multiple radio components without core emission, such as our case, an identification was sought at the centre of the source. The relic GRG without a radio core presented in this study has been assigned a reliable optical counterpart at optical position RA =  $02^{\text{h}} 16^{\text{m}} 59^{\text{s}}.064$ , Dec. =  $-04^{\circ} 49' 20''.85$  with spectroscopically measured redshift  $z_{\text{spec}} \sim 1.325$  (see table 3 in Simpson et al. 2006). The identified host galaxy of the relic GRG is a very red galaxy ( $R - z' = 2.0$ ) and resides almost exactly midway between the radio lobes. Figure 2 shows overlay of 0.325 GHz radio contours on the optical three-colour RGB image obtained by combining Subaru  $B$  band (blue),  $R$  band (green) and  $z'$  band (red) images. Optical magnitudes of the host galaxy in  $B$ ,  $V$ ,  $R$ ,  $i'$  and  $z'$  bands from Simpson et al. (2006) are listed in Table 1. The host galaxy is also detected in near-

**Table 1.** AB magnitudes of the host galaxy in the optical and IR bands.

Band	<i>B</i>	<i>V</i>	<i>R</i>	<i>i'</i>	<i>z'</i>	<i>J</i>	<i>H</i>	<i>K</i>	3.6 $\mu$ m	4.5 $\mu$ m	5.8 $\mu$ m	8 $\mu$ m
Magnitude	25.08	24.62	23.96	22.98	22.02	20.30	19.23	18.13	17.83	17.91	18.66	19.23

*Note.* Optical band magnitudes (*B*, *V*, *R*, *i'*, *z'*) are from Subaru data (Simpson et al. 2006), near-IR fluxes (*J*, *H*, *K*) are from the UKIDSS-UDS catalogue and mid-infrared fluxes (3.6, 4.5, 5.6, 8 $\mu$ m) were measured from the SpUDS images within a fixed circular aperture of 6.0 arcsec diameter.

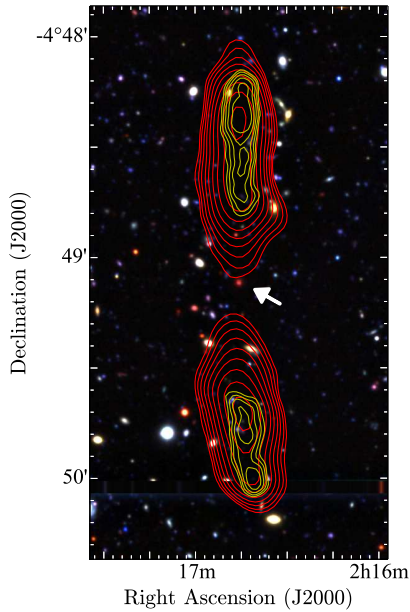


**Figure 2.** 0.325 GHz (in red) and 1.4 GHz (in yellow) radio contours overlaid on the three-colour optical RGB image. RGB three-colour image obtained by combining Subaru *B* band (blue), *R* band (green) and *z'* band (red) images. The extreme red colour of the host galaxy is apparent in RGB image. The arrow points to the host galaxy. Both 0.325 and 1.4 GHz contours start from  $5\sigma$  and increase in steps of  $\sqrt{2} \times \sigma$ .

IR (*J*, *H* and *K* bands) and mid-IR (3.6, 4.5, 5.8 and 8  $\mu$ m) bands observed as a part of UK Infrared Deep Sky Survey (UKIDSS) Ultra Deep Survey (UDS; Lawrence et al. 2007) and *Spitzer* UKIDSS Ultra Deep Survey (SpUDS; PI: James S. Dunlop)<sup>1</sup>, respectively.

## 2.4 Photometric redshift of the host galaxy

The spectroscopic redshift of the extremely red host galaxy provided by Simpson et al. (2006) is based on a low S/N spectrum from FOCAS/Subaru. In order to check the reliability of spectroscopic redshift, we estimated photometric redshift using 12 band photometric data (*B*, *V*, *R*, *i'* and *z'* band from Subaru, *J*, *H*, *K* band from UKIDSS and 3.6, 4.5, 5.0 and 8.0  $\mu$ m from SpUDS). We estimated the photometric redshift ( $z_{\text{phot}}$ ) of the host by fitting template SEDs to the photometric data using the publicly available

photometric redshift estimation code EAZY<sup>2</sup> (Brammer et al. 2008). We obtain  $z_{\text{phot}} = 1.26^{+0.10}_{-0.03}$ , similar to the spectroscopic redshift,  $z_{\text{spec}} = 1.325$ , within  $1\sigma$ . Our  $z_{\text{phot}}$  is also consistent with  $z_{\text{phot}}$  in the range 0.98 — 1.174 reported by Vardoulaki et al. (2008) using relatively shallow mid-IR data from SWIRE. Our estimated  $z_{\text{phot}}$  independently confirms the  $z_{\text{spec}}$  estimate to be reliable. We use  $z_{\text{spec}} = 1.325$  for our calculations.

## 3 RADIO PROPERTIES

### 3.1 Radio morphology

We detect the two radio lobes in both the 0.325 and 1.4 GHz images, while the AGN core, jets and/or hotspots remain undetected. The non-detection of AGN core, jets and hotspots classifies this source to be a relic radio galaxy (e.g., Murgia et al. 2011; Saripalli et al. 2012).

At 0.325 GHz, the total integrated flux density of the relic GRG J021659-044920 is  $140 \pm 6.9$  mJy with northern and southern lobes having integrated flux densities of  $79.8 \pm 5.2$  mJy and  $60.2 \pm 4.5$  mJy, respectively. In Table 2, we list the flux densities of the GRG at various radio frequencies. The total angular extent at 0.325 GHz (within  $5\sigma$  contour) is 2.4 arcmin and corresponds to a projected linear size of  $\sim 1.2$  Mpc at redshift 1.325. The projected linear sizes of northern and southern lobes at 0.325 GHz are  $\sim 600$  kpc (1.18 arcmin) and  $\sim 510$  kpc (1 arcmin), respectively. At 1.4 GHz the source size is relatively smaller with total end-to-end projected linear size of 1.1 Mpc (2.26 arcmin). The total integrated flux density at 1.4 GHz is  $9.60 \pm 0.14$  mJy with northern and southern lobes having  $5.8 \pm 0.1$  mJy and  $3.80 \pm 0.09$  mJy, respectively. Using  $5\sigma$  rms noise as the upper limit for the undetected AGN core, we estimate the core-to-lobe flux density ratio to be  $\lesssim 1$  and  $\lesssim 5$  per cent at 1.4 and 0.325 GHz, respectively. This low value of core-to-lobe flux density ratio is similar to other relic GRGs (see e.g., Hurley-Walker et al. 2015).

### 3.2 Radio spectrum and spectral index map

In Figure 3 (left-hand panel), we show the radio spectrum for the GRG J021659-044920 between 0.24 and 1.4 GHz. We list the radio spectral indices computed across 0.240, 0.325, 0.610 and 1.4 GHz in Table 2. The solid line shows

<sup>1</sup> <http://irsa.ipac.caltech.edu/data/SPITZER/SpUDS/>

<sup>2</sup> <http://www.astro.yale.edu/ezay/>



**Table 2.** Radio flux densities and spectral indices of relic GRG J021659-044920. Column 1: flux density at 1.4 GHz measured using Simpson et al. (2006) image. Column 2 is 0.610 GHz flux density of the GRG taken from Vardoulaki et al. (2008). Column 3 is 0.325 GHz flux density measured using our 0.325 GHz image. Column 4 is 0.240 GHz flux density of the GRG taken from Tasse et al. (2007). Columns 5, 6, 7 and 8 are spectral indices between 1.4 to 0.610 GHz, 1.4 to 0.325 GHz, 0.610 to 0.325 GHz and 0.325 to 0.240 GHz, respectively. All flux densities are integrated within  $5\sigma$  contours.

	1.4 GHz (mJy) (1)	0.610 GHz (mJy) (2)	0.325 GHz (mJy) (3)	0.240 GHz (mJy) (4)	$\alpha_{0.610}^{1.4 \text{ GHz}}$ (5)	$\alpha_{0.325}^{1.4 \text{ GHz}}$ (6)	$\alpha_{0.325}^{0.610 \text{ GHz}}$ (7)	$\alpha_{0.240}^{0.325 \text{ GHz}}$ (8)
North lobe	5.80±0.10	—	79.8±5.20			1.79±0.11		
South lobe	3.80±0.09	—	60.2±4.52			1.89±0.12		
Total	9.60±0.14	>43.3	140±6.9	169.1±20.2	> 1.81	1.83±0.08	< 1.86	0.6±0.5

the best-fitting spectrum fitted by a power-law with exponential cutoff. We describe the spectral modelling in Section 3.3. It is evident that the radio spectrum is convex and steepens sharply above 0.325 GHz. The source shows strong spectral evolution from 0.240 to 1.4 GHz. The radio spectral index estimated between 0.325 and 1.4 GHz is  $\alpha \sim 1.8$ , consistent with fading lobes without injection of fresh particles from AGN. In the literature, radio spectral curvature is computed as the difference between high-frequency spectral index and low-frequency spectral index (i.e.,  $\alpha_{\text{high}} - \alpha_{\text{low}}$ ).  $\alpha_{\text{high}} - \alpha_{\text{low}} \geq 1.0$  has been used as a criterion to selected relic (dying) radio galaxies (e.g., Murgia et al. 2011). With this criterion our source having radio spectral curvature ( $\alpha_{0.610}^{1.4 \text{ GHz}} - \alpha_{0.240}^{0.325 \text{ GHz}}$ ) > 1.19, can be categorized as a dying radio galaxy. In the active phase, radio galaxies generally show radio spectra represented by a power-law over a wide range of frequencies. However, in the absence of fresh particle injection during the relic phase, the energy spectrum of the synchrotron emitting relativistic electrons develop an exponential cut-off towards higher energies due to synchrotron and/or IC losses. This leads to an cut-off in the high frequency radio spectrum. Therefore, the fading lobes in relic GRG are expected to show very steep ( $\alpha > 1.3$ ) and convex radio spectra, characteristic of electron population that has radiated away much of the energy (Komissarov & Gubanov 1994).

In Figure 3 (right-hand panel), we present the spectral index map computed between 0.325 and 1.4 GHz using pixels above  $3\sigma$  at both the frequencies. The 0.325 GHz emission extends well beyond 1.4 GHz emission in the lobes. Spectral index varies from 1.4 to 2.5 with gradual steepening in the lobes from outer extremities to inner regions towards the host galaxy. The average spectral index of the northern lobe is  $\sim 1.8$ , and that of the southern lobe is  $\sim 1.9$  (see Table 2). The spectral index is extremely steep relative to typical low- $z$  radio galaxies where it is  $\sim 0.7$  (Blundell et al. 1999). However, the variation of spectral index with distance from the nucleus in the lobes is consistent with the backflow model of the lobes (Leahy & Williams 1984; Leahy et al. 1989). According to this model, pressure in the hotspot re-accelerates the post-shock material back towards the core, creating a backflow. Thus, the part of the lobe closer to the host galaxy consists of an older population of cosmic ray electrons (CREs) that are backflowed and makes the radio continuum spectrum steep in those regions.

### 3.3 Energy losses

The relativistic electrons in the radio lobes undergo energy losses that modifies the power-law radio spectrum. The dominant energy loss processes are synchrotron, IC and adiabatic cooling. Synchrotron and IC losses have the effect of steepening the spectrum and leads to a cutoff at higher radio frequencies ( $\gtrsim 1$  GHz), while adiabatic losses affect the normalization of the spectrum but not its curvature. In the following we suppose that the radiative losses are the dominant energy loss process for the relativistic electrons. We neglect the effect of the expansion losses as this is a dying source and perhaps in equilibrium with external pressure.

Both, synchrotron and IC losses affect the spectrum in similar ways, whereby, the spectrum is smoothly steepened at higher frequencies. The spectrum is characterized by a break frequency,  $\nu_{\text{br}}$ , below which the spectrum remains a power-law with a spectral index identical to the injection spectral index ( $\alpha_{\text{inj}}$ ). Above  $\nu_{\text{br}}$ , the form of the steepening depends on the mechanism of particle injection. For steady continuous injection of relativistic electrons (CI model), the spectrum steepens by 0.5 (Pacholczyk 1970). For single shot particle injection, the spectrum falls off as a power-law with index  $4\alpha_{\text{inj}}/3 + 1$  above the break frequency, assuming constant pitch angle between electrons and magnetic field (KP model; Kardashev 1962; Pacholczyk 1970). However, considering rapid isotropization of the pitch angle distribution leads to an exponential cut-off above the break frequency (JP model; Jaffe & Perola 1973).

In Figure 4 we show the expected spectral index between rest-frame 0.76 and 3.25 GHz (corresponding to 0.325 and 1.4 GHz in the observed frame) as a function of the break frequency in the rest frame ( $\nu_{\text{br,rest}}$ ) for the different models described above. We assumed an injection spectral index  $\alpha_{\text{inj}} = 0.5$ , and produced synthetic radio spectrum for varying  $\nu_{\text{br,rest}}$ . The shaded region shows the observed range of spectral index in the lobes. Clearly, the CI model cannot produce the observed steepness and would require  $\alpha_{\text{inj}} > 1$ , which is generally not the case. The fact that the extended radio emission is very bright at low radio frequencies and extends well beyond high frequency radio emission together with the observed spectral index supports the fact that the lobes consists of an old population of electrons that were injected into the intergalactic medium (IGM) from a now discontinued jet activity.

From Figure 4, we find that the observed steepening of the spectral index can be produced by the JP model. As per

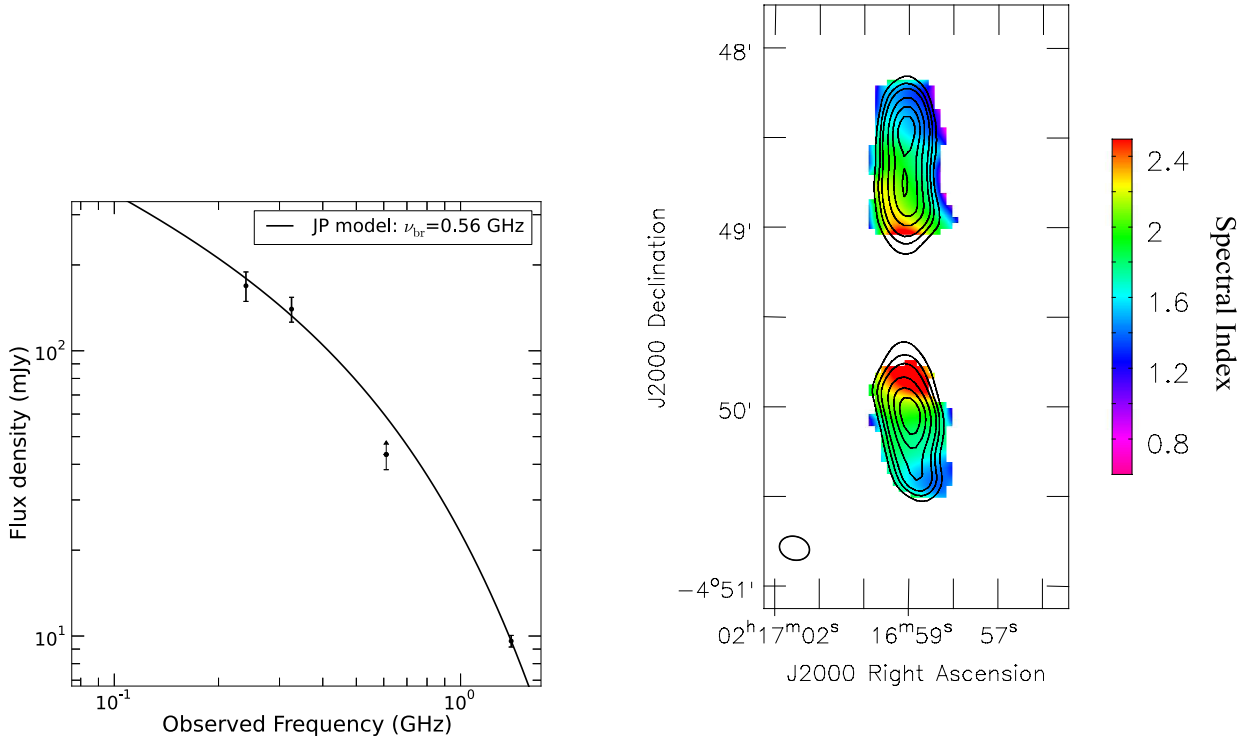


**Figure 3.** Left-hand panel: integrated radio continuum spectrum between 0.24 and 1.4 GHz of the relic GRG. The spectrum is fitted using the JP model for synchrotron radiative loss. Right-hand panel: spectral index map of the GRG estimated between 0.325 and 1.4 GHz using  $3\sigma$  flux density levels. Overlaid are the 0.325 GHz total intensity contours.

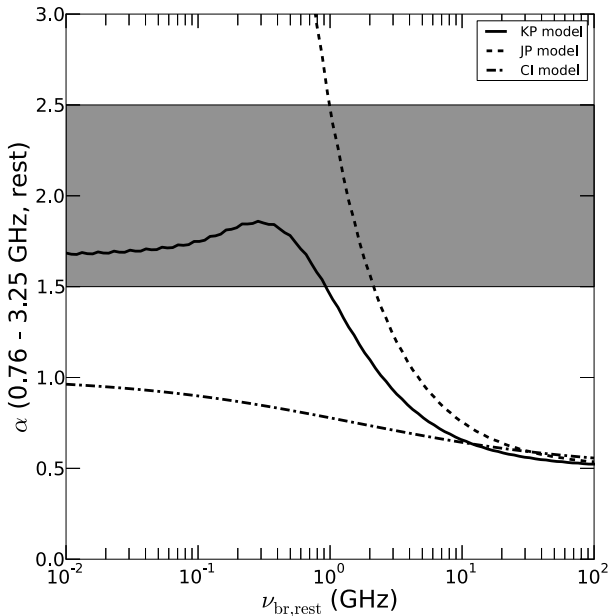


**Figure 4.** Expected spectral index between rest-frame 0.76 and 3.25 GHz as a function of the break frequency at rest frame,  $\nu_{\text{br,rest}}$  for the various models of particle injection with  $\alpha_{\text{inj}} = 0.5$ . The shaded region shows the observed range of spectral index in the lobes.

the JP model, the range of spectral index suggests,  $\nu_{\text{br,rest}}$  to be in the range 1–2.2 GHz in the rest frame. We therefore model the observed radio spectrum using the JP model. However, we note that, the JP spectrum with a single  $\nu_{\text{br}}$  is better represented for localized regions. The total radio emission is a sum of several JP spectra having a range of  $\nu_{\text{br}}$ . Depending on the time since first injection, i.e., the total age of the source ( $t_s$ ) and the time elapsed since injection switch-off ( $t_{\text{off}}$ ), the  $\nu_{\text{br}}$  lies in the range  $\nu_{\text{br,low}}$  and  $\nu_{\text{br,high}}$ , respectively. Here,  $t_s = t_{\text{off}} + t_{\text{on}}$ , where,  $t_{\text{on}}$  is the duration of the active phase. The two break frequencies are related as,  $\nu_{\text{br,high}} = \nu_{\text{br,low}}(t_s/t_{\text{off}})^2$  (see Murgia et al. (2011)). In the scenario, where the dying phase is longer than that of the active phase, i.e.  $t_{\text{off}} \gg t_{\text{on}}$ , the two break frequencies overlap and the global spectrum can be represented by a JP model consisting of a single break frequency. In our case, the spectrum is not sampled enough to determine the two break frequencies. We therefore model the spectrum by a single  $\nu_{\text{br}}$  and approximate the JP spectrum as  $S_\nu = A\nu^{-\alpha_{\text{inj}}}e^{-\nu/\nu_{\text{br}}}$ . Here,  $A$  is the normalization at 1 GHz and  $\alpha_{\text{inj}}$  is the injection spectral index. Under this assumption, the  $\nu_{\text{br}}$  is determined by  $t_s$ . We assume, a typical value of  $\alpha_{\text{inj}}$  to be 0.5. We fit the above form for the JP model to the observed radio continuum spectra between 0.24 and 1.4 GHz. For our data, we find  $\nu_{\text{br}} = 0.57 \pm 0.02$  GHz, i.e.,  $\nu_{\text{br,rest}} = 1.32$  GHz and is consistent with what is expected from Figure 4. The best-fitting radio spectrum is shown as the solid line in Figure 3 (left-hand panel).

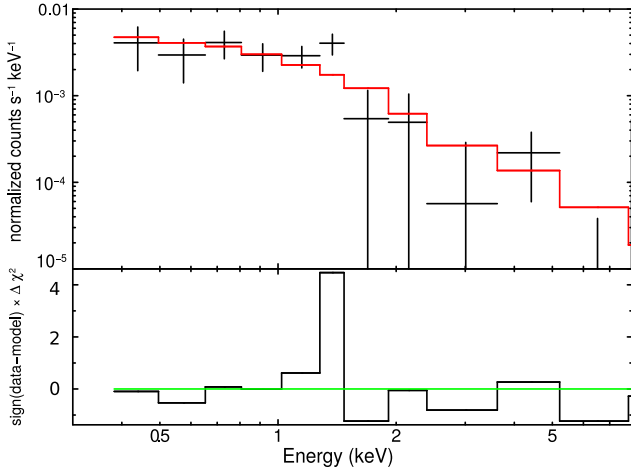


**Figure 5.** 0.3 — 10 keV *XMM-Newton* PN spectrum best fitted with an absorbed power-law, where absorbing column density is fixed to the Galactic value. Solid red line and crosses (‘+’) represent fitted model and binned data points, respectively. Residuals are shown in the bottom panel.

## 4 X-RAY PROPERTIES

### 4.1 X-ray data reduction

We performed X-ray data reduction using Science Analysis System (SAS) version 13.5 and followed standard procedure outlined in the *XMM-Newton* ABC Guide<sup>3</sup>. We processed raw Observations Data Files by using SAS tasks `emproc` and `epproc`, for the MOS and PN data. We use latest calibration files to obtain calibrated and concatenated event lists. These files were filtered for flaring particle background time intervals using standard recommended `PATTERN`, `FLAG` and energy filters to generate clean event lists. From clean calibrated data files we extracted source and background spectra. Source spectrum was extracted by choosing two elliptical regions covering X-ray emission from each of the two lobes. The counts are not sufficient to obtain robust spectral fits for individual lobes, and therefore, we opted to extract source spectrum covering both the lobes. The background spectrum is extracted using a source-free annular region in the same chip. The response matrix file and the ancillary response file were created using the SAS tasks `RMFGEN` and `ARFGEN`, respectively. The spectra were grouped to a minimum of 20 counts per bin in order to use  $\chi^2$  fitting statistics. The MOS and PN data are consistent with each other but PN data are slightly better at higher energies  $> 2.0$  keV and therefore, we present spectral fitting using the PN data only.

### 4.2 X-ray spectral fitting and analysis

To study the nature of X-ray emission from lobes we fitted the 0.3 — 10 keV EPIC PN spectrum using physically motivated models. We use the X-ray spectral fitting package `XSPEC` version 12.8.2 (Arnaud 1996) to fit the X-ray spectrum. Since the relic GRG has no AGN core emission, we fit the 0.3 — 10 keV spectrum with a single absorbed power-law of the form,  $M(E) = K e^{-N_H \sigma(E)} E^{-\Gamma}$ . Here,  $K$  is the

normalization of the emission at 1 keV,  $N_H$  is the absorbing column density between source and observer,  $\sigma(E)$  is the photoelectric absorption cross-section (ignoring Thomson scattering) and  $\Gamma$  is the photon index of the power-law. We get  $N_H = 2.42^{+5.31}_{-2.47} \times 10^{21} \text{ cm}^{-2}$ ,  $\Gamma = 2.99^{+3.13}_{-1.38}$  and  $\chi^2/\text{dof} = 7.7/10 \sim 0.77$ . Keeping all the parameters free does not constrain  $\Gamma$ . However, by fixing the absorbing column density equal to the Galactic value ( $N_H = 2.52 \times 10^{20} \text{ cm}^{-2}$ ) statistically improves the fit with  $\chi^2/\text{dof} = 9.7/11 \sim 0.88$  and better constrains  $\Gamma$  to be  $1.86^{+0.49}_{-0.41}$ . We use this value of  $\Gamma$  in our further analysis. The 0.3 — 10 keV EPIC PN spectrum fitted with absorbed power-law model for fixed  $N_H$  is shown in Figure 5 and the best-fitting parameters are listed in Table 3.

To investigate the possibility of thermal origin of X-ray emission from hot diffuse gas present in the cluster medium, we also fitted the 0.3 — 10 keV spectrum with a thermal plasma model (`MEKAL`). The `MEKAL` model represents an emission spectrum from hot diffuse gas based on the model calculations of Mewe et al. (1986). The `MEKAL` model with multiplicative Galactic absorption component does not render a statistically good fit if all the parameters are kept free. We tried fixing the metal abundance of the hot gas in the cluster medium in the `MEKAL` model from 0.1 to 1.5 of Solar values in steps of 0.1 but found unphysical or unconstrained plasma temperatures (see Table 3). Therefore, it is unlikely that X-ray emission from the lobes are of thermal origin. In fact, the extended X-ray morphology nearly co-spatial with the radio lobes precludes it from being due to hot cluster gas. Murgia et al. (2012) reported that relic radio galaxies residing in cluster environments display large scale diffuse X-ray emission having spherical morphology. And, the X-ray emission is characterized by thermal emission from hot gas present in the cluster. We note that Finoguenov et al. (2010) present a list of X-ray emitting clusters in the SXDF but the X-ray emission in our source is reported to be mainly from radio lobes. Therefore, we conclude that the observed X-ray emission is non-thermal in origin and perhaps originates due to IC scattering of the CMB photons (ICCMB).

## 5 CONNECTION BETWEEN RADIO AND X-RAY EMISSION

The co-spatial nature of the radio synchrotron and the soft X-rays emission from the lobes suggests a fundamental connection between the emitting particle populations within the lobes. A possible scenario is IC scattering of CMB photons by CREs having Lorentz factors,  $\gamma_e \gtrsim 10^3$ , wherein the CMB photons are upscattered to X-ray wavebands. Depending on the magnetic field strengths, CREs with  $\gamma_e \sim 10^2 - 10^5$  give rise to synchrotron emission in the radio wavebands between  $\sim 10$  MHz and 100 GHz. However, due to radiative losses, the lifetime of relativistic electrons are inversely proportional to  $\gamma_e$ . Thus, the radiative lifetimes of (highly energetic) radio synchrotron-emitting electrons are shorter than the (less energetic) electrons which give IC emission in the X-ray band. As a consequence, IC emission always traces an older population of particles which may be more diffuse and spatially non-coincident with the radio emission. This gives rise to smaller extent and larger off-set between the radio emission from the lobes at 1.4 GHz and the X-ray emission

<sup>3</sup> <https://heasarc.gsfc.nasa.gov/docs/xmm/abc/>

**Table 3.** Best-fitting parameters for the power-law and MEKAL models. Errors represent 90 per cent confidence interval on all parameters.

Model	Parameter	Value
power-law	$K_{\text{norm}}$	$5.29^{+1.30}_{-1.30} \times 10^{-6}$
	$N_{\text{H}}$ ( $\text{cm}^{-2}$ ) (fixed)	$2.52 \times 10^{20}$
	$\Gamma$	$1.86^{+0.49}_{-0.41}$
	$\chi^2/\text{dof}$	9.7/11
	0.3 — 10 keV flux <sup>1</sup>	$3.25 \times 10^{-14}$
	2.0 — 10 keV flux <sup>2</sup>	$1.50 \times 10^{-14}$
MEKAL	$K_{\text{norm}}$	$7.90^{+1.09}_{-1.93} \times 10^{-5}$
	$kT$ (keV)	$4.2^{+15.3}_{-2.3}$
	$n_{\text{H}}$ ( $\text{cm}^{-3}$ )	$1.17 \times 10^{-2}$
	Abundance	0.6
	$\chi^2/\text{dof}$	9.27/10

<sup>1</sup> Observed frame unabsorbed flux in  $\text{erg cm}^{-2} \text{s}^{-1}$ .<sup>2</sup> Rest frame unabsorbed flux in  $\text{erg cm}^{-2} \text{s}^{-1}$ .

(see Figure 1). This is because, at 1.4 GHz the emission is produced by a population of relatively short-lived higher energy electrons as compared to the 0.325 GHz emission.

The equivalent magnetic field for IC scattering with CMB,  $B_{\text{IC}}$ , is given by  $\approx 3.25(1+z)^2 \mu\text{G}$ . For the GRG,  $B_{\text{IC}} \approx 17.5 \mu\text{G}$  is significantly stronger than that of the estimated magnetic field of  $\sim 3.3 \mu\text{G}$  (see Section 6.1) indicating IC losses significantly dominates over the synchrotron losses. This is because the IC cooling time-scale for electrons radiating at 1.4 GHz (i.e., 3.25 GHz in the rest frame) in a magnetic field strength of  $3.3 \mu\text{G}$  is  $\sim 4.8 \times 10^6$  yrs, significantly lower than that of the synchrotron cooling timescale of  $\sim 1.2 \times 10^8$  yr. Thus, the radio emission from the lobes of the GRG are strongly affected by IC losses.

The power-law nature of the X-ray emission from the lobes can arise due to synchrotron emission from highly energetic electrons having  $\gamma_e \sim 2.7 \times 10^8$  at 2 keV (4.65 keV in the rest frame). Such electrons have radiative (synchrotron + IC) lifetime of  $\sim 2.5 \times 10^2$  yr in a magnetic field of  $\sim 3.3 \mu\text{G}$  at  $z = 1.325$ . This is about four orders of magnitude lower than the estimated spectral age of  $\sim 8 \times 10^6$  yr in the lobes (see Section 6.3). We therefore conclude that, the X-ray emission is a direct consequence of IC scattering of the CMB photons with the CREs emitting in the radio frequencies.

Under ICCMB, it is expected that the non-thermal X-ray spectrum will have similar spectral shape as of the radio spectrum if the IC X-ray and synchrotron radio emission are produced due to the same population of electrons. This implies that the spectral index in the radio should be the same as the slope of the X-ray spectrum. In our observations, we find that the radio spectral index,  $\alpha$  to be in the range 1.4 – 2.5 (see Figure 3). The X-ray emission photon index ( $\Gamma$ ) is related to the X-ray spectral index ( $\alpha_{\text{Xray}}$ ) as  $\alpha_{\text{Xray}} = \Gamma - 1$ . Our estimated value of  $\Gamma = 1.86^{+0.49}_{-0.41}$  corresponds to  $\alpha_{\text{Xray}} = 0.86^{+0.23}_{-0.12}$ , significantly flatter than that of the radio spectral index estimated between the observed frequencies (see Section 3.2).

In terms of energy, electrons emitting between 0.76 and

3.25 GHz in the rest frame (i.e., 0.325 and 1.4 GHz in the observed frame), correspond to the energy range  $\sim 3.6 - 7.6$  GeV for magnetic field strengths of  $3.3 \mu\text{G}$ . Thus,  $\gamma_e$  of the electrons are  $\sim 7 \times 10^3$  and  $\sim 1.5 \times 10^4$ , respectively. For CMB photons at  $z = 1.325$ , having temperature 6.34 K, the Planck function peaks at  $\nu_{\text{bg}} \approx 6.6 \times 10^{11}$  Hz. These photons are up-scattered by the CREs in the radio to X-ray frequencies with average frequencies given by  $\langle \nu \rangle \approx (4/3)\gamma^2 \nu_{\text{bg}}$ . Thus, the CREs emitting at rest frame 0.76 and 3.25 GHz would up-scatter these CMB photons to  $\sim 4.3 \times 10^{19}$  and  $\sim 2 \times 10^{20}$  Hz, i.e., in the energy range  $\sim 175$  and 830 keV. Therefore, our X-ray observations between  $\sim 0.3$  and 10 keV, corresponding to  $\sim 0.7$  and 23.25 keV in the rest frame, do not probe this steep part of the spectrum. In our observed range of X-ray energies, the emission arises due to IC scattering from CREs at much lower energies ( $\gamma_e \sim 5 \times 10^2 - 1.8 \times 10^3$ ) corresponding to lower radio frequencies where the spectral index is expected to be significantly flatter than that between rest frame 0.76 and 3.25 GHz. In this way, the different spectral indices as measured in the X-ray and radio observations can be explained.

## 6 MAGNETIC FIELD STRENGTH AND AGE OF THE RELIC LOBES

### 6.1 Magnetic field strengths

Together with radio observations, the ICCMB X-ray fluxes can be used to constrain the magnetic field strength in the lobes of radio galaxies (e.g., [Erlund et al. 2006](#)). We use the formula given in [Tucker \(1977\)](#) to estimate the magnetic field in the lobes as,

$$\frac{F_c}{F_s} = 2.47 \times 10^{-19} (5.23 \times 10^3)^\alpha \left( \frac{T_{\text{CMB}}}{\text{K}} \right)^{3+\alpha} \times \frac{b(n)}{a(n)} \left( \frac{B}{\text{G}} \right)^{-(\alpha+1)} \left( \frac{\nu_c}{\nu_s} \right)^{-\alpha}. \quad (1)$$

Here,  $F_c$  and  $F_s$  are the flux of the X-ray and radio emission, respectively,  $T_{\text{CMB}}$  is the temperature of the CMB at the redshift of the source,  $\nu_c$  is the frequency of IC X-ray emission,  $\nu_s$  is the frequency of radio synchrotron emission and the constants  $a(n)$  and  $b(n)$  are taken from [Ginzburg & Syrovatskii \(1965\)](#) and [Tucker \(1977\)](#), respectively.

This analysis requires the observed X-ray and radio fluxes to be co-spatial. To get the co-spatial flux, we extracted the source spectrum in a region matching the  $5\sigma$  contours of the 0.325 GHz image, and fitted the spectrum with an absorbed power-law model with  $N_{\text{H}}$  set to Galactic absorption. The best-fitting photon index is found to be  $\Gamma = 1.77^{+0.51}_{-0.42}$  corresponding to spectral index of  $0.77^{+0.22}_{-0.18}$ . The co-spatial, unabsorbed, 2 — 10 keV rest frame X-ray flux is  $1.44 \times 10^{-14} \text{ erg s}^{-1} \text{ cm}^{-2}$  that corresponds to 0.75 nJy. For a synchrotron flux density  $F_s = 140 \text{ mJy}$  at  $\nu_s = 0.325$  GHz,  $\alpha = 0.77$  and  $h\nu_c \approx 3 \text{ keV}$ , we estimate the  $B$  to be  $\sim 3.3 \mu\text{G}$ .

### 6.2 Energy equipartition

We also compute the magnetic field strength assuming equipartition of energy between CREs and magnetic field



(see Moffet 1975, equation 2.77). We use the 0.325 GHz emission, where the radio-emitting lobes of the GRG are assumed to be cylindrical in shape,  $\sim 500$  kpc long and  $\sim 180$  kpc in diameter each. The synchrotron cutoff frequencies are assumed to be  $\nu_{\min} = 10$  MHz and  $\nu_{\max} = 10$  GHz. We neglect the contribution of relativistic protons to the total energy of relativistic particles in our calculations. Note that, the 1.4 GHz flux density is heavily affected by ICCMB losses. This analysis is valid only for synchrotron losses. Therefore, the observed spectral index of 1.83 between 0.325 and 1.4 GHz would give rise to magnetic field strengths that are overestimated and would also be sensitive to the choice of lower frequency cut-off. We therefore assume a typical spectral index for synchrotron losses as 1.0. Using these values, we estimate the equipartition magnetic field strength,  $B_{\text{eq}} \sim 3.5 \mu\text{G}$  in the lobes.

The equipartition magnetic field strength and the magnetic field strength derived using the X-ray and radio emission agrees well with each other indicating the energy equipartition to be valid in the lobes of the GRG.

The energy equipartition can be independently tested by comparing the total energies in the estimated magnetic field strength and the relativistic electrons ( $\mathcal{E}_e$ ) (see e.g., Isobe et al. 2011). We find the unabsorbed 2 — 10 keV rest frame X-ray luminosity of the lobes to be  $1.64 \times 10^{44} \text{ erg s}^{-1}$ , consistent with typical luminosities of other GRGs (Erlund et al. (6C 0905+39; 2008), Laskar et al. (3C 469.1; 2010)). Using the X-ray luminosity, we estimate the minimum energy in the relativistic electrons ( $\mathcal{E}_e$ ) following equation 4 in Erlund et al. (2006),

$$\mathcal{E}_e = \frac{3}{4} \frac{L_{44}}{\gamma_e(1+z)^4} 10^{64} \text{ erg.} \quad (2)$$

Here,  $L_{44}$  is the X-ray luminosity in units of  $10^{44} \text{ erg s}^{-1}$  and  $\gamma_e$  is the typical Lorentz factor of the electrons responsible for ICCMB. Assuming  $\gamma_e = 10^3$ , we find  $\mathcal{E}_e = 4.2 \times 10^{59} \text{ erg}$ . The total magnetic field energy ( $\mathcal{E}_B$ ) in the lobes for  $B \sim 3.3 \mu\text{G}$ , within a cylindrical volume of  $\sim 180$  kpc diameter and a total length of  $\sim 1$  Mpc is  $\sim 6.4 \times 10^{59} \text{ erg}$ . The two energies match within  $\sim 30$  per cent, indicating energy equipartition to be valid. Similar equipartition of energy has been observed for the GRG DA 240 by Isobe et al. (2011). Further, we note that the minimum energy in the relativistic electrons for the GRG is similar to other powerful high redshift Fanaroff–Riley type II radio galaxies (see e.g., Erlund et al. 2006). It shows that the ICCMB electrons that are longer lived than their radio emitting synchrotron counterparts can deposit a significant amount of energy into their surrounding IGM.

### 6.3 Age of the relic

The observed radio spectrum is well modelled by the JP model, discussed in Section 3.3. In this case,  $\nu_{\text{br}}$  depends on the total age of the electrons ( $t_s$ ) and the magnetic field strength ( $B$ ) as

$$\frac{\nu_{\text{br}}}{\text{GHz}} = 1.12 \times 10^{15} \left( \frac{B}{\text{G}} \right) \left[ \frac{2}{3} \left\{ \left( \frac{B}{\text{G}} \right)^2 + \left( \frac{B_{\text{IC}}}{\text{G}} \right)^2 \right\} \left( \frac{t}{\text{s}} \right) \right]^{-2}. \quad (3)$$

Thus, for our estimated value of magnetic field strength

of  $\sim 3.3 \mu\text{G}$  and  $\nu_{\text{br,rest}} = 1.32 \text{ GHz}$ , using Equation 3, we find the age of the relativistic electrons in the lobes and hence the age of the relic to be  $t_s \sim 8 \times 10^6 \text{ yr}$ , which is typical for relic GRGs (Murgia et al. 2011).

## 7 SUMMARY

We report the discovery of a relic GRG J021659-044920 at redshift ( $z$ )  $\sim 1.325$  with extended diffuse X-ray emission, nearly co-spatial with the radio lobes. The salient properties of this GRGs are as below.

(i) The radio lobes are best detected at low radio frequencies observed using the GMRT at 0.325 GHz. The total angular extent at 0.325 GHz is 2.4 arcmin that corresponds to a projected linear size of  $\sim 1.2$  Mpc at the redshift of the source.

(ii) The host galaxy is identified in deep optical (Subaru), near-IR (UKIDSS) and mid-IR (SpUDS). It is a red ( $R - z' = 2.0$ ) and dusty galaxy that brightens in mid-IR bands.

(iii) The relic nature of the radio galaxy is evident as the AGN core, jets and/or hotspots remain undetected and the lobes exhibits a very steep radio spectral index,  $\alpha_{0.325 \text{ GHz}}^{1.4 \text{ GHz}} \sim 1.4 - 2.5$ . The 0.24—1.4 GHz radio spectrum of the lobe emission is convex and steepens sharply above 0.325 GHz due to radiative losses. The spectral index of the lobes, estimated between 0.325 and 1.4 GHz, varies from 1.4 in the outer edges to 2.5 in the inner regions, suggesting backflow of plasma.

(iv) The X-ray spectrum between 0.3 and 10 keV is best fitted by an absorbed power-law model with photon index,  $\Gamma = 1.86_{-0.41}^{+0.49}$  for a fixed absorbing column density similar to the Galactic value. The comparison of radio and X-ray spectral and morphological properties suggests that X-ray emission is likely due to inverse-Comptonization of CMB photons by low energy electrons compared to electrons radiating at 0.325 — 1.4 GHz frequencies.

(v) Using the ICCMB X-ray emission, we estimate the lower limit for the total energy in relativistic electrons to be  $\sim 4.2 \times 10^{59} \text{ erg}$  (for  $\gamma_e \sim 10^3$ ), implying significant feedback from GRG into the surrounding IGM.

(vi) The magnetic field strength estimated using X-ray and radio emission and by energy equipartition yield consistent field strengths of  $\sim 3.5 \mu\text{G}$ . This suggests that the energy equipartition between magnetic field and relativistic electrons to be valid in the GRG.

## ACKNOWLEDGEMENTS

We gratefully acknowledge generous support from the Indo–French Center for the Promotion of Advanced Research (Centre Franco- Indien pour la Promotion de la Recherche Avancée) under programme no. 4404–3. We thank Sui Ann Mao, Rainer Beck, Nirupam Roy and Dharam Vir Lal for critically reviewing the manuscript and giving constructive and supportive suggestions. We thank Chris Simpson for providing the 1.4-GHz VLA radio image of the SXDF field. We thank Alain Omont for useful comments on an early draft of this manuscript. We thank the anonymous referee for carefully reading the manuscript and giving useful comments and suggestions. The GMRT is run

by the National Centre for Radio Astrophysics of the Tata Institute of Fundamental Research. The National Radio Astronomy Observatory is a facility of the National Science Foundation operated under cooperative agreement by Associated Universities, Inc. This paper is based in part on observations obtained with *XMM–Newton* (an ESA science mission with instruments and contributions directly funded by ESA Member States and the USA, NASA). This paper is partially based on data collected at Subaru Telescope, which is operated by the National Astronomical Observatory of Japan. This work is based in part on data obtained as part of the UKIRT Infrared Deep Sky Survey. This work is based in part on observations made with the *Spitzer* Space Telescope, which is operated by the Jet Propulsion Laboratory (JPL), California Institute of Technology (Caltech), under a contract with NASA.

## REFERENCES

- Arnaud K. A., 1996, in Jacoby G. H., Barnes J., eds, *Astronomical Society of the Pacific Conference Series Vol. 101, Astronomical Data Analysis Software and Systems V*, p. 17
- Basu A., Wadadekar Y., Beelen A., Singh V., Archana K. N., Sirothia S., Ishwara-Chandra C. H., 2015, *ApJ*, **803**, 51
- Begelman M. C., Blandford R. D., Rees M. J., 1984, *Reviews of Modern Physics*, **56**, 255
- Blundell K. M., Rawlings S., Willott C. J., 1999, *AJ*, **117**, 677
- Blundell K. M., Fabian A. C., Crawford C. S., Erlund M. C., Celotti A., 2006, *ApJ*, **644**, L13
- Brammer G. B., van Dokkum P. G., Coppi P., 2008, *ApJ*, **686**, 1503
- Bridle A. H., Perley R. A., 1984, *ARA&A*, **22**, 319
- Cordey R. A., 1987, *MNRAS*, **227**, 695
- Erlund M. C., Fabian A. C., Blundell K. M., Celotti A., Crawford C. S., 2006, *MNRAS*, **371**, 29
- Erlund M. C., Fabian A. C., Blundell K. M., 2008, *MNRAS*, **386**, 1774
- Fabian A. C., Sanders J. S., Crawford C. S., Etori S., 2003, *MNRAS*, **341**, 729
- Fabian A. C., Chapman S., Casey C. M., Bauer F., Blundell K. M., 2009, *MNRAS*, **395**, L67
- Finoguenov A., et al., 2010, *MNRAS*, **403**, 2063
- Ginzburg V. L., Syrovatskii S. I., 1965, *ARA&A*, **3**, 297
- Hurley-Walker N., et al., 2015, *MNRAS*, **447**, 2468
- Isobe N., Seta H., Tashiro M. S., 2011, *PASJ*, **63**, 947
- Jaffe W. J., Perola G. C., 1973, *A&A*, **26**, 423
- Johnson O., Almaini O., Best P. N., Dunlop J., 2007, *MNRAS*, **376**, 151
- Kardashev N. S., 1962, *SvA*, **6**, 317
- Komissarov S. S., Gubanov A. G., 1994, *A&A*, **285**, 27
- Laskar T., Fabian A. C., Blundell K. M., Erlund M. C., 2010, *MNRAS*, **401**, 1500
- Lawrence A., et al., 2007, *MNRAS*, **379**, 1599
- Leahy J. P., Williams A. G., 1984, *MNRAS*, **210**, 929
- Leahy J. P., Muxlow T. W. B., Stephens P. W., 1989, *MNRAS*, **239**, 401
- Mauduit J.-C., et al., 2012, *PASP*, **124**, 714
- Mewe R., Lemen J. R., van den Oord G. H. J., 1986, *A&AS*, **65**, 511
- Moffet A. T., 1975, *Strong Nonthermal Radio Emission from Galaxies*, the University of Chicago Press, p. 211
- Murgia M., Parma P., de Ruiter H. R., Mack K.-H., Fanti R., 2005, in Sjouwerman L. O., Dyer K. K., eds, *X-Ray and Radio Connections*, p. 8 ([arXiv:astro-ph/0405091](https://arxiv.org/abs/astro-ph/0405091))
- Murgia M., et al., 2011, *A&A*, **526**, A148
- Murgia M., Markevitch M., Govoni F., Parma P., Fanti R., de Ruiter H. R., Mack K.-H., 2012, *A&A*, **548**, A75
- Pacholczyk A. G., 1970, *Radio astrophysics. Nonthermal processes in galactic and extragalactic sources*
- Parma P., Murgia M., de Ruiter H. R., Fanti R., Mack K.-H., Govoni F., 2007, *A&A*, **470**, 875
- Saripalli L., Hunstead R. W., Subrahmanyan R., Boyce E., 2005, *AJ*, **130**, 896
- Saripalli L., Subrahmanyan R., Thorat K., Ekers R. D., Hunstead R. W., Johnston H. M., Sadler E. M., 2012, *ApJS*, **199**, 27
- Scharf C., Smail I., Ivison R., Bower R., van Breugel W., Reuland M., 2003, *ApJ*, **596**, 105
- Scheuer P. A. G., 1974, *MNRAS*, **166**, 513
- Simpson C., et al., 2006, *MNRAS*, **372**, 741
- Singh V., et al., 2014, *A&A*, **569**, A52
- Strüder L., et al., 2001, *A&A*, **365**, L18
- Tasse C., Röttgering H. J. A., Best P. N., Cohen A. S., Pierre M., Wilman R., 2007, *A&A*, **471**, 1105
- Tucker W. H., 1977, *Radiation processes in astrophysics*.
- Turner M. J. L., et al., 2001, *A&A*, **365**, L27
- Ueda Y., et al., 2008, *ApJS*, **179**, 124
- Vardoulaki E., Rawlings S., Simpson C., Bonfield D. G., Ivison R. J., Ibar E., 2008, *MNRAS*, **387**, 505
- Venturi T., Bardelli S., Morganti R., Hunstead R. W., 1998, *MNRAS*, **298**, 1113

This paper has been typeset from a  $\text{\LaTeX}$  file prepared by the author.